Subwavelength metal-optic semiconductor nanopatch lasers

Kyoungsik Yu,[1,2] Amit Lakhani,[1] and Ming C. Wu[1,*]

[1]*Department of Electrical Engineering and Computer Sciences, University of California, Berkeley, CA 94720, USA*
[2]*Currently with the Department of Electrical Engineering, KAIST (Korea Advanced Institute of Science and Technology), Daejeon 305-701, Korea*
*wu@eecs.berkeley.edu

Abstract: We report on near infrared semiconductor nanopatch lasers with subwavelength-scale physical dimensions (0.019 cubic wavelengths) and effective mode volumes (0.0017 cubic wavelengths). We observe lasing in the two most fundamental optical modes which resemble oscillating electrical and magnetic dipoles. The ultra-small laser volume is achieved with the presence of nanoscale metal patches which suppress electromagnetic radiation into free-space and convert a leaky cavity into a highly-confined subwavelength optical resonator. Such ultra-small lasers with metallodielectric cavities will enable broad applications in data storage, biological sensing, and on-chip optical communication.

References and links

1. D. A. B. Miller, "Device requirements for optical interconnects to silicon chips," Proc. IEEE **97**, 1166–1185 (2009).
2. R. G. Beausoleil, P. J. Kuekes, G. S. Snider, S. Y. Wang, and R. S. Williams, "Nanoelectronic and nanophotonic interconnect," Proc. IEEE **96**(2), 230–247 (2008).
3. L. Pan, and D. B. Bogy, "Data storage: Heat-assisted magnetic recording," Nat. Photonics **3**(4), 189–190 (2009).
4. M. Lončar, A. Scherer, and Y. M. Qiu, "Photonic crystal laser sources for chemical detection," Appl. Phys. Lett. **82**(26), 4648–4650 (2003).
5. Y. Nakayama, P. J. Pauzauskie, A. Radenovic, R. M. Onorato, R. J. Saykally, J. Liphardt, and P. D. Yang, "Tunable nanowire nonlinear optical probe," Nature **447**(7148), 1098–1101 (2007).
6. O. Painter, R. K. Lee, A. Scherer, A. Yariv, J. D. O'Brien, P. D. Dapkus, and I. Kim, "Two-dimensional photonic band-Gap defect mode laser," Science **284**(5421), 1819–1821 (1999).
7. H. G. Park, S. H. Kim, S. H. Kwon, Y. G. Ju, J. K. Yang, J. H. Baek, S. B. Kim, and Y. H. Lee, "Electrically driven single-cell photonic crystal laser," Science **305**(5689), 1444–1447 (2004).
8. K. Nozaki, S. Kita, and T. Baba, "Room temperature continuous wave operation and controlled spontaneous emission in ultrasmall photonic crystal nanolaser," Opt. Express **15**(12), 7506–7514 (2007).
9. Q. Song, H. Cao, S. T. Ho, and G. S. Solomon, "Near-IR subwavelength microdisk lasers," Appl. Phys. Lett. **94**(6), 061109 (2009).
10. M. T. Hill, Y. S. Oei, B. Smalbrugge, Y. Zhu, T. De Vries, P. J. Van Veldhoven, F. W. M. Van Otten, T. J. Eijkemans, J. P. Turkiewicz, H. De Waardt, E. J. Geluk, S. H. Kwon, Y. H. Lee, R. Notzel, and M. K. Smit, "Lasing in metallic-coated nanocavities," Nat. Photonics **1**(10), 589–594 (2007).
11. M. T. Hill, M. Marell, E. S. P. Leong, B. Smalbrugge, Y. C. Zhu, M. H. Sun, P. J. van Veldhoven, E. J. Geluk, F. Karouta, Y. S. Oei, R. Nötzel, C. Z. Ning, and M. K. Smit, "Lasing in metal-insulator-metal sub-wavelength plasmonic waveguides," Opt. Express **17**(13), 11107–11112 (2009).
12. M. H. Huang, S. Mao, H. Feick, H. Q. Yan, Y. Y. Wu, H. Kind, E. Weber, R. Russo, and P. D. Yang, "Room-temperature ultraviolet nanowire nanolasers," Science **292**(5523), 1897–1899 (2001).
13. X. F. Duan, Y. Huang, R. Agarwal, and C. M. Lieber, "Single-nanowire electrically driven lasers," Nature **421**(6920), 241–245 (2003).
14. R. F. Oulton, V. J. Sorger, T. Zentgraf, R.-M. Ma, C. Gladden, L. Dai, G. Bartal, and X. Zhang, "Plasmon lasers at deep subwavelength scale," Nature **461**(7264), 629–632 (2009).
15. M. A. Noginov, G. Zhu, A. M. Belgrave, R. Bakker, V. M. Shalaev, E. E. Narimanov, S. Stout, E. Herz, T. Suteewong, and U. Wiesner, "Demonstration of a spaser-based nanolaser," Nature **460**(7259), 1110–1112 (2009).
16. T. Baba, "Photonic crystals and microdisk cavities based on GaInAsP-InP system," IEEE J. Sel. Top. Quantum Electron. **3**(3), 808–830 (1997).

17. D. Kajfez, and P. Guillon, *Dielectric resonators*, The Artech House microwave library (Artech House, Dedham, MA, 1986).
18. C. Manolatou, and F. Rana, "Subwavelength nanopatch cavities for semiconductor plasmon lasers," IEEE J. Quantum Electron. **44**(5), 435–447 (2008).
19. E. Feigenbaum, and M. Orenstein, "Optical 3D cavity modes below the diffraction-limit using slow-wave surface-plasmon-polaritons," Opt. Express **15**(5), 2607–2612 (2007).
20. S. B. Cohn, "Microwave bandpass filters containing high-Q dielectric resonators," IEEE Trans. Microw. Theory Tech. **16**(4), 218–227 (1968).
21. Z. H. Zhu, H. Liu, S. M. Wang, T. Li, J. X. Cao, W. M. Ye, X. D. Yuan, and S. N. Zhu, "Optically pumped nanolaser based on two magnetic plasmon resonance modes," Appl. Phys. Lett. **94**(10), 103106 (2009).
22. P. B. Johnson, and R. W. Christy, "Optical-constants of noble-metals," Phys. Rev. B **6**(12), 4370–4379 (1972).
23. J. P. Berenger, "A perfectly matched layer for the absorption of electromagnetic-waves," J. Comput. Phys. **114**(2), 185–200 (1994).
24. E. M. Purcell, "Spontaneous emission probabilities at radio frequencies," Phys. Rev. **69**, 681–681 (1946).
25. L. A. Coldren, and S. W. Corzine, *Diode lasers and photonic integrated circuits* (Wiley-Interscience, New York, NY, 1995).
26. T. Baba, T. Hamano, F. Koyama, and K. Iga, "Spontaneous emission factor of a microcavity DBR surface-emitting laser," IEEE J. Quantum Electron. **27**(6), 1347–1358 (1991).
27. H. Y. Ryu, M. Notomi, E. Kuramoti, and T. Segawa, "Large spontaneous emission factor (> 0.1) in the photonic crystal monopole-mode laser," Appl. Phys. Lett. **84**(7), 1067–1069 (2004).
28. B. Min, E. Ostby, V. Sorger, E. Ulin-Avila, L. Yang, X. Zhang, and K. Vahala, "High-Q surface-plasmon-polariton whispering-gallery microcavity," Nature **457**(7228), 455–458 (2009).
29. A. Mizrahi, V. Lomakin, B. A. Slutsky, M. P. Nezhad, L. Feng, and Y. Fainman, "Low threshold gain metal coated laser nanoresonators," Opt. Lett. **33**(11), 1261–1263 (2008).
30. F. Wang, and Y. R. Shen, "General properties of local plasmons in metal nanostructures," Phys. Rev. Lett. **97**(20), 206806 (2006).
31. J. C. Ho, R. Yerushalmi, Z. A. Jacobson, Z. Fan, R. L. Alley, and A. Javey, "Controlled nanoscale doping of semiconductors via molecular monolayers," Nat. Mater. **7**(1), 62–67 (2008).

1. Introduction

Coherent light sources with subwavelength length scales are of considerable interest in view of their applications in optical interconnects [1, 2], data storage [3], biological/chemical sensing [4], and imaging [5]. Semiconductor lasers with subwavelength volume are particularly interesting because their sizes start to approach those of transistors in silicon integrated circuits. Several novel semiconductor laser structures have been experimentally demonstrated to reduce laser sizes, including photonic crystals [6–8], microdisks [9], metal-clad cavities [10,11], nanowires [5, 12, 13], and hybrid metal-nanowire waveguides [14]. However, focus has only been put on reducing physical laser sizes in only one or two dimensions, although such subwavelength lasers may find their greatest applications when they are physically small. Reducing the third dimension remains the most difficult challenge as radiation and/or ohmic losses increase rapidly. Recently, Noginov *et al.* reported a deep-subwavelength laser based on modified Cornell dots [15]; however the use of dye molecules as the gain material precludes electrical pumping or high-speed modulation.

In this paper, we report on subwavelength-scale semiconductor lasers in the near infrared using cylindrical metallodielectric nanopatch resonators. We observe lasing in the two most fundamental optical modes, which resemble oscillating electrical and magnetic dipoles. The physical volume of the nanopatch laser is only 0.019 cubic wavelength (0.056 μm^3 at 1420 nm wavelength). The laser diameter and thickness are 406 and 440 nm, respectively, and the longest dimension of the laser is only 0.3 wavelengths. The total mass of the laser is less than 0.6 picograms.

2. Laser and cavity design

The nanopatch semiconductor laser structure is shown schematically in Fig. 1a. A cylindrical semiconductor gain medium is sandwiched between a circular metal patch and a ground plane. The scanning electron micrograph of a typical finished device is shown in Fig. 1b. The size and shape of the circular metallic patches, which defines the resonant wavelength, is precisely controlled by electron-beam lithography. The radius, r, is varied from 200 to 310 nm, and the total thickness of the semiconductor and dielectric layers between the metal planes is h=230 nm. Indium gallium arsenide phosphide (InGaAsP) is used as the

semiconductor gain material since phosphide-based materials are known to have low surface recombination velocities; reduction of nonradiative recombination at the etched sidewalls is paramount to obtaining a high-efficiency laser with a high surface-to-volume ratio [16]. Gold is used for both metal layers, and its thickness is approximately 80 nm. The metal thickness is chosen to be much larger than the field penetration depth (Δ) at the near infrared region, and the resonator properties do not change much with thicker metal layers according to our simulations.
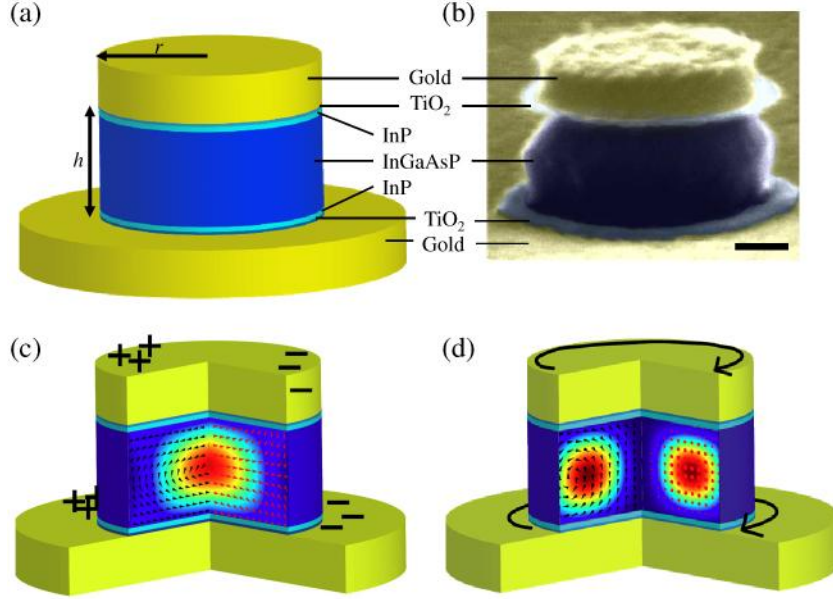

Fig. 1. Structure and mode profiles of the nanopatch semiconductor laser. (a) Schematic drawing and (b) scanning electron micrograph of a metallodielectric nanopatch semiconductor laser. The scale bar represents 100 nm. (c, d) Computed mode profiles for the two lowest order modes: the electrical dipole mode (TM_{111}, c) and the second-order magnetic dipole mode (TE_{011}, d). The surface color at the cross-section represents the electrical energy density, and the arrows show the direction of the electric (red) and magnetic (black) field. The nanopatch radius and height are $r = 250$ nm and $h = 230$ nm, respectively. The effective modal volumes are $0.54(\lambda_{TM}/2n_{eff})^3$ and $2.99(\lambda_{TE}/2n_{eff})^3$, where n_{eff} is the effective refractive index of the dielectric layers. In the metal layers, free charges (c) and currents (d) arise to satisfy the boundary condition at the metal-dielectric interfaces.

Albeit in the optical frequency, the cylindrical nanopatch resonators can be approximately modeled using ideal boundary conditions with perfect electric conductors (PEC) at the dielectric-metal interface and a perfect magnetic conductor at the semiconductor sidewall [17]. Similar nanopatch resonator designs have been theoretically investigated recently [18, 19]. The radius and height of the cylindrical cavity model are r and $h+2\Delta$, respectively. Under the first-order Cohn model [17, 20], the cavity resonance wavelength for the TM_{mnp} mode is given by

$$\lambda_{TM_{mnp}} = \frac{2\pi\sqrt{\varepsilon}}{\sqrt{\left(\dfrac{\chi'_{mn}}{r}\right)^2 + \left(\dfrac{p\pi}{h+2\Delta_{TM_{mnp}}}\right)^2}}. \tag{1}$$

χ'_{mn} represents the nth root of the derivative of the mth Bessel function of the first kind, ε is the average permittivity of the dielectric region, and m, n, and p stand for azimuthal, radial, and axial mode number, respectively. In general, m, n, and p are non-negative integers. However, due to the PEC boundary, the axial mode number, p, cannot be 0 (p=1, 2, 3, …).

Since the smallest root of the Bessel functions and their derivatives is $\chi'_{11} \approx 1.841$, the fundamental eigenmode with a moderate quality factor among the TM_{mnp} and TE_{mnp} modes is the TM_{111} mode that resembles oscillating electrical dipoles. Electric field lines are almost linearly polarized and mostly terminate on free charges in the metal layers as indicated in Fig. 1c. Most of the optical mode energy is thus confined to the middle of the gain region, resulting in a high confinement factor of 84%. Since the radiation is significantly suppressed, most of the optical energy is lost from resistive heating in the metal. Although such optical losses practically set an upper bound of the cavity quality factor, it is still larger than pure dielectric microdisk resonators with the same subwavelength dimensions [9].

Since the cavity height ($h =230$ nm and $\Delta \approx 10$ nm) is comparable to or less than the nanopatch radii for our experiments, the second-order mode is a TE_{011}-like magnetic dipole mode described in Fig. 1d. This corresponds to a whispering-gallery-like mode with an azimuthal mode number of 0 and a radial mode number of 1, and it is commonly called a monopole mode in photonic crystal slab resonators [7, 8]. Unlike the linearly-polarized electric dipole mode, a strong axial magnetic field is present at the resonator center, and the electric field circulates around it with a donut shape, signifying the presence of a magnetic dipole along the longitudinal axis. For this second-order mode, the radiation is not completely suppressed, but the mode overlaps less with the metal layers than the electric dipole mode. As a result, the overall quality factor and the effective mode volume are both larger than the electric dipole mode. The magnetic dipole mode is nondegenerate while the electric dipole mode is doubly degenerate in two orthogonal directions.

3. Nanopatch laser fabrication and characterization

3.1. Device fabrication

The semiconductor nanopatch lasers were fabricated by metal evaporation, substrate removal, electron-beam lithography, and anisotropic etching processes. A 200 nm-thick $In_{0.4}Ga_{0.6}As_{0.85}P_{0.15}$ bulk gain layer sandwiched by 10 nm-thick InP barriers was first grown on an InP substrate. Atomic layer deposition (ALD) was then used to grow 5 nm of TiO_2 layer to limit carrier tunneling into metal, since the thin InP barriers were insufficient to confine the carriers. A Ti/Au/Ti metal layer was subsequently evaporated with thicknesses of 3 nm/80 nm/20 nm. The metal thickness is chosen to be much larger than the field penetration depth (Δ) at the near infrared region, and the resonator's properties do not change much with thicker metal layers according to our simulations. After metal evaporation, the samples were bonded to a carrier wafer. The InP substrate was then removed with $HCl:H_3PO_4$ etchant. ALD was used again to deposit an additional 5 nm of TiO_2 onto the InP barrier layer after completely removing the substrate. Metal evaporation of Ti/Au/Ti (3 nm/80 nm/20 nm) was performed again to create the second metal plane, which corresponds to the upper metal plane in Fig. 1. Electron-beam lithography was used to define circular hardmask patterns in hydrogen silsesquioxane resist (XR-1541, Dow Corning). The sample was then milled with an argon ion beam accelerated to ~1 kV to pattern the metal film, and then subsequently etched with reactive ion etching with a combination of H_2 and CH_4 gases. Finally, the damaged semiconductor surface was chemically etched using self-limiting surface redox reactions. The damaged sidewall surface was first oxidized, and then subsequently etched in 49% aqueous hydrofluoric acid solution. To eliminate possible interaction between lasers, the distance between adjacent devices was designed to be 10 μm, which is much larger than the cavity eigenmode volume, the pump/laser wavelength, and the pump beam spot size.

3.2. Device measurement and characterization

To reduce metal loss and non-radiative recombination and increase the semiconductor optical gain, we performed our laser characterization at low temperature (78K). The fabricated sample was mounted in a low temperature cryostat cooled by liquid nitrogen, and optically pumped from the top by a 1060 nm semiconductor diode laser with a 100 ns pulse width and a 5 kHz repetition rate (0.05% duty cycle) using a microscope objective with a 0.7 numerical

aperture. The excitation pulse width of 100 ns is chosen to be much larger than the spontaneous emission and carrier lifetimes, which are on the order of one nanosecond, to obtain quasi-static equilibrium during the pumping time. Low duty cycle pulses are used to minimize possible thermal effects. However, thermal gradients in time most likely affected the emission characteristics of each lasing mode, broadening the measured linewidth from its actual value. This problem was exacerbated by inefficient pumping of the cavity from the top of the nanopatch cavity. The diameter of the focused pump beam is approximately 2 μm. The photoluminescence emission spectra at various optical excitation powers and positions were captured by the same objective used to pump the laser, and analyzed by an infrared spectrometer. The dependence of the spectrally-integrated laser power as a function of the excitation power was obtained from the spectra data. For polarization-resolved near-field radiation pattern measurements, a high-sensitivity InGaAs near-infrared camera was placed at the image plane of the objective, and a broadband linear polarizer in front of the camera selected a single polarization. A zero-order quarter-wave plate was also used to identify the polarization state of the near-field radiation.

4. Results

Figure 2 shows the resonant wavelength evolution and lasing spectra of the metallodielectric nanopatch cavities with various radii. The cavity resonance dispersion of the two lowest order modes is clearly observed (Fig. 2a), and agrees well with the analytic model (Eq. (1), solid line) and numerical simulations based on finite-difference time-domain (FDTD, dashed line) [18]. The mode-dependent penetration depths were adjusted to obtain the best fit with the experimental observations (Δ_{TM111}=13 nm and Δ_{TE011}=8 nm). Gold was modeled by using an experimentally found frequency-dependent complex dielectric constant at room temperature [22]. Titanium layers are neglected in our simulation. Frequency dependent refractive indices are also used for semiconductor layers. The refractive index of TiO_2 was set to 2.4. Although this value is uncertain and depends on the atomic layer deposition quality, the sensitivity of TiO_2 index variation is minimal since most of the electromagnetic field is confined to the semiconductor region. According to our simulation results, the exact shape of sidewall also does not play a significant role in the mode frequency as the electromagnetic field is concentrated in the middle of the semiconductor structure.
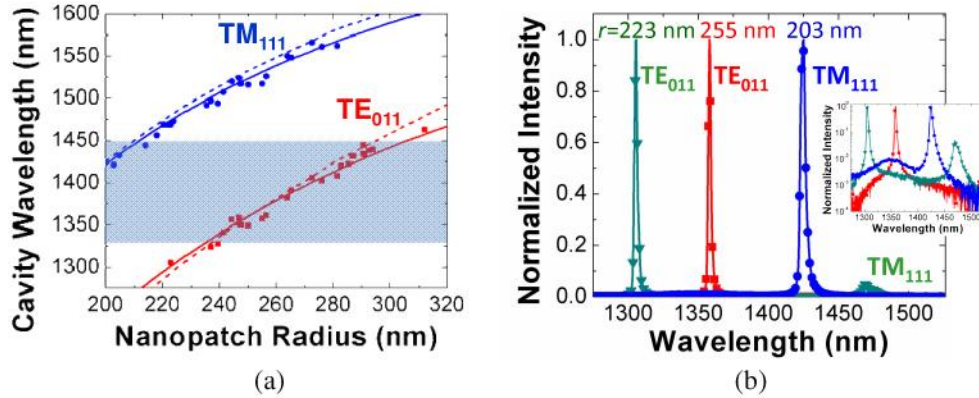

Fig. 2. Spectral properties and near-field radiation patterns of the nanopatch laser. (a) Resonance wavelengths of the metallodielectric nanopatch cavities with different radii at low temperature (78 K). The scattered points represent measurement results, the dashed lines represent numerical modeling, and the solid lines are the theoretical dispersion curves for electrical (TM$_{111}$, penetration depth Δ_{TM111}=13 nm, blue) and magnetic (TE$_{011}$, Δ_{TE011}=8 nm, red) dipole mode from the perfect conductor model. The colored region shows the gain spectra full width at half maximum. (b) Laser emission spectra for three different nanopatch sizes (r = 203, 223, 255 nm). The inset shows the log-scale plot.

We observed single-mode lasing with > 20 dB side-mode suppression for most cavity radii (Fig. 2b). Small nanopatch cavities ($r<215$ nm) lase in the electric dipole mode, while larger cavities lase dominantly in the magnetic dipole mode. Cavities with intermediate sizes exhibit significant side mode emission because the gain spectrum overlaps with both modes ($r=223$ nm in Fig. 2b). Although higher order modes are also observed at energies greater than the magnetic dipole mode in large-diameter cavities, no lasing action is seen because their quality factors are too low in accord with predictions from numerical simulations.
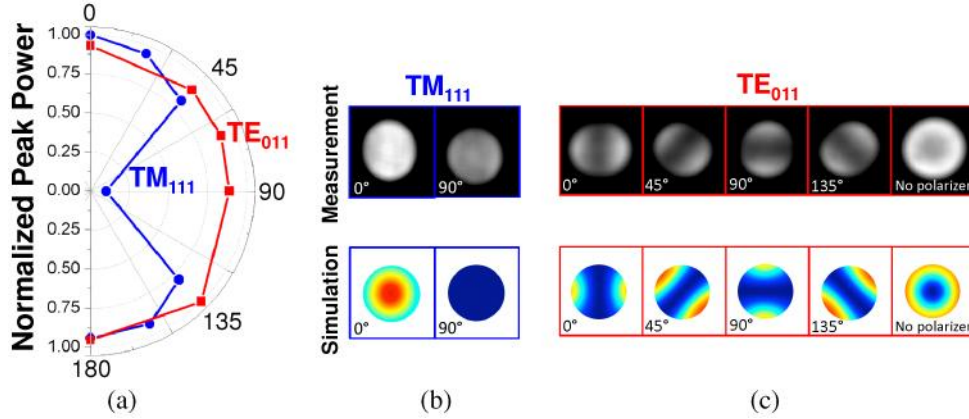

Fig. 3. (a) Normalized peak power with respect to the linear polarization angle for the electrical (blue, circles) and magnetic (red, squares) dipole modes. The measured near-field radiation patterns with various polarization angles shown in (b) and (c) confirm that the first and second-order modes are linearly and azimuthally polarized, respectively (grayscale images in the upper row). They also agree well with the FDTD simulations (color images in the lower row).

Polarization-resolved near-field imaging reveals that the electric dipole mode is linearly polarized with a surface-normal radiation pattern, whereas the magnetic dipole mode is azimuthally polarized and has a ring-shaped radiation pattern within the objective's numerical aperture (Fig. 3). In the far field regime, the electric dipole mode primarily radiates surface normal, and the magnetic dipole mode radiates in-plane with the device, making it more suitable for integration with planar lightwave circuit technologies.
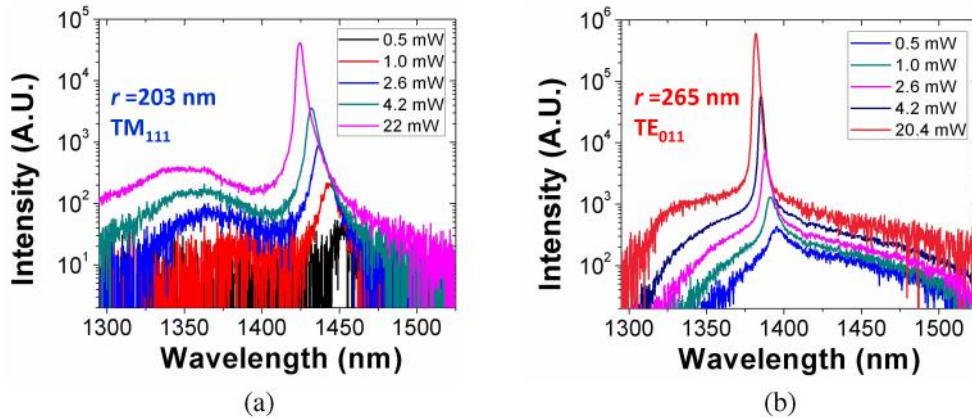

Fig. 4. Evolution of the emission spectra with increasing peak pump power for nanopatch lasers with radius of (a) 203 and (b) 265 nm. The 203-nm nanopatch cavity lases in electric dipole mode while the 265-nm cavity lases in magnetic dipole mode.

The laser emission spectra were measured at various optical pumping levels for two representative nanopatch lasers which mainly support the electrical (TM_{111}, $r=203$ nm) and

magnetic (TE_{011}, r=265 nm) dipole modes. Figures 4a and 4b show examples of such measurements. A small fraction of optical pumping energy from the surface normal direction is transferred to the gain medium mainly by scattering near the cavity structure. Since most of pumping energy is reflected by the patch and ground plane, it is difficult to accurately estimate the actual absorbed pump power at the gain material. We therefore use the total optical pump power incident on the sample in Figs. 4 and 5. We estimate that only a small fraction of pump power is coupled to the subwavelength-scale nanopatch resonator structure (λ_{pump}=1060 nm), and the actual absorbed pump power is much lower. The optical pumping efficiency can be increased by making the cavity resonant with the pump light [21].

5. Discussion

5.1. Cavity quality factor

The cavity quality factors for the electric and magnetic dipole modes are experimentally estimated to be 132 and 168, respectively, from the emission spectra well below the laser threshold. FDTD numerical simulations based on room-temperature metal loss predict quality factors of 65 and 80, which is approximately half of the experimental values. We believe that this discrepancy can be explained by the reduction in resistive heating in the metal layers at low temperature [10]. The cavity quality factors measured at room temperature also show similar trends. The complex permittivities of our evaporated gold films were characterized using ellipsometry from 200 to 800 nm wavelength at room temperature, and the data agreed very well with the values published in the literature [22].

The energy loss of metallodielectric cavities is dominated by radiation and metallic loss, so the total cavity quality factor can be decomposed as $Q_{tot}^{-1}=Q_{rad}^{-1}+Q_{loss}^{-1}$. The radiation quality factor, Q_{rad}, can be found by setting the imaginary part of the metal permittivity to be zero in computer simulations and thereby removing the resistive metallic loss. A perfectly matched layer was used to absorb all radiation from the cavity [23]. It was found that the total quality factor of the electric dipole mode was $Q_{total,\,TM}$=65, while $Q_{rad,\,TM}$~1600. Therefore, losses in this mode were dominated mainly by energy dissipation in the metal layers. For the TE_{011} mode, the quality factors were found to be $Q_{total,\,TE}$=80 and $Q_{rad,\,TE}$=205, indicating more efficient radiation from the cavity.

5.2. Effective mode volume

The effective mode volumes, V_{eff}, for the electric and magnetic dipole modes, estimated from simulations, are $0.54(\lambda_{TM}/2n_{eff})^3$ and $2.99(\lambda_{TE}/2n_{eff})^3$, respectively, where n_{eff} is the effective refractive index of the laser cavity. All of the electric field within the whole simulation volume was considered, and the electromagnetic energy contained in the metal layers was taken into account by using the relation ε_{metal}=d($\omega\varepsilon$)/dω. The effective modal volume of the TE_{011}-like magnetic dipole mode is comparable to that of other previously reported monopole whispering gallery modes in the near-infrared region [8], although the nanopatch's physical size is much smaller. We also found that the normalized modal volumes do not vary much with the cavity size and corresponding resonance wavelength.

Since not all dipole emitters are located in the electric field maximum, an alternate definition of the modal volume can be obtained by replacing the maximum electric energy density in the denominator with the average energy density over the gain volume [10]. The average modal volumes, V_{ave}, for the electric and magnetic dipole modes are found to be $1.45(\lambda/2n)^3$ and $7.44(\lambda/2n)^3$, respectively. However, since carrier diffusion within the material will allow carriers to migrate to regions of high spontaneous recombination rates, the true mode volume for the Purcell factor calculation will most likely fall between the conventional effective modal volume, V_{eff}, and the averaged modal volume, V_{ave} [10].

5.3. Effective spontaneous emission enhancement (Fβ product)

With such small mode volumes, the spontaneous emission from the gain medium is usually modified through the Purcell effect [24]. Our optical cavity linewidth is broader than the

homogeneous linewidth of the bulk gain material at typical pump levels, which is about a few milli-electron-volt at low temperature. The Purcell factor for a particular polarization is given by $F=(2/\pi^2)Q/(V_{eff}/(\lambda/2n_{eff})^3)$ [16]. From the experimental quality factors (Q) and calculated modal volumes ($V_{eff}/(\lambda/2n_{eff})^3$), the Purcell factors for the electrical and magnetic dipole modes are calculated to be 49.5 (λ_{TM}=1420 nm) and 11.4 (λ_{TE}=1380 nm), respectively.
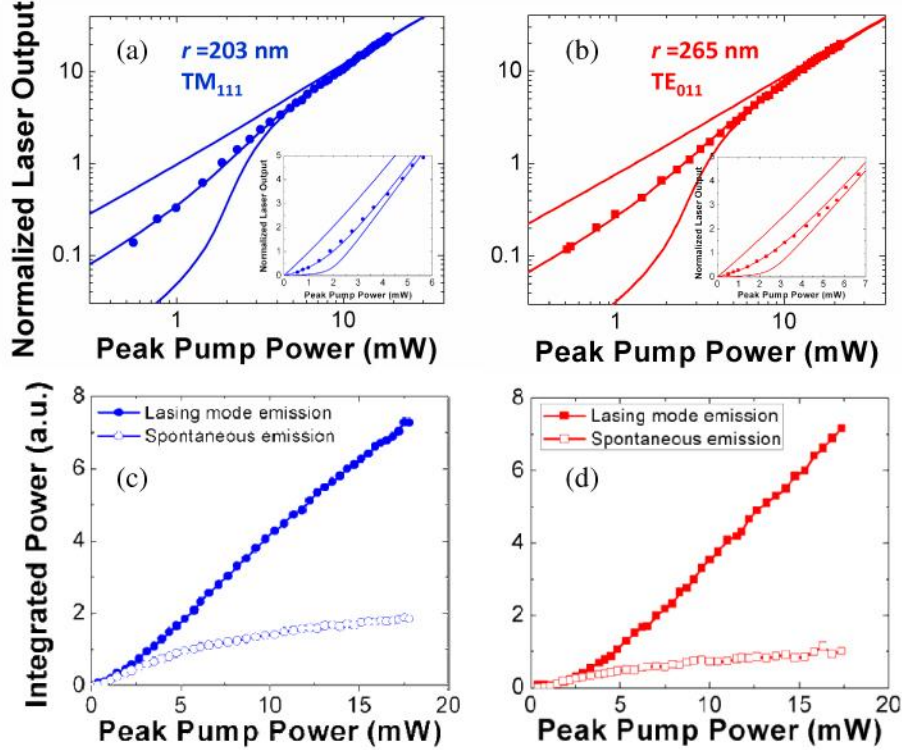

Fig. 5. Output intensity characteristics of the nanopatch lasers. Output intensity-versus-pump characteristics of the semiconductor nanopatch lasers with radius of (a, c) 203 and (b, d) 265 nm. Stimulated and spontaneous emission components are separately shown in (c, d), while total output powers are plotted in (a, b). The solid lines in (a, b) are simulations obtained from the laser rate equation with the Purcell factor, F, and spontaneous emission coupling factor, β. Output intensity curves for $F\beta$=0.1 and 10 are also shown for comparison. The insets in (a, b) show the linear-scale plots near the laser threshold. The vertical scales are normalized by the laser output powers at threshold pump levels predicted by the rate equation models. The parameters used for the electric and magnetic dipole modes are F=49.5, β=0.022 and F=11.4, β=0.105, respectively.

To evaluate the spontaneous emission coupling factor, β, of the nanopatch lasers with respect to their eigenmodes, the experimental luminescence data are compared with theoretical curves obtained from the following rate equations [25].

$$\frac{dN}{dt} = P - gS - \frac{1-\beta}{\tau_{sp}}N - \frac{F\beta}{\tau_{sp}}N - \frac{v_s S_a}{V_a}N$$

$$\frac{dS}{dt} = \Gamma gS - \frac{S}{\tau_{ph}} + \frac{\Gamma F\beta}{\tau_{sp}}N$$

(2)

N and S are the carrier and photon densities, P is the pumping rate, N_0 is the transparent carrier density, and Γ is the optical confinement factor. S_a and V_a are the exposed surface area and volume of the gain region, respectively ($S_a=2\pi rh$, $V_a=\pi r^2 h$). Steady-state solutions are used to obtain the fitting curves in Fig. 5. The spontaneous emission lifetime is assumed to be

τ_{sp}=1.5 ns, and the laser mode has faster spontaneous emission rate accelerated by the Purcell factor, F. We only considered surface recombination as a non-radiative recombination source because Auger recombination is negligible at low temperature. When assuming a surface recombination velocity of v_s=2×10^4 cm/s, the non-radiative recombination lifetime is ~one nanosecond with the given cavity radius (r=200~300 nm). The photon lifetime is important in determining the laser threshold and is assumed to be proportional to the cavity quality factor (τ_{ph}=$Q/(2\pi f)$), where Q and f are the cavity quality factor and resonance frequency, respectively). Since the carrier concentration, N, is not much larger than the transparent carrier density, N_0, we assumed a linear model for optical gain g=$cG(N-N_0)/n_g$=$1.09×10^{-5}(N-4×10^{17})$ s^{-1}, where c, n_g, and G represent the light velocity in vacuum, the group refractive index of the cavity, and the linear differential gain coefficient, respectively.

The small effective mode volume and the good optical mode confinement in the gain material result in relatively large β and strong photon-cavity interactions. As a result, the integrated laser emission power behavior near threshold is very gradual, but the light output slope changes are still noticeable as shown in the insets of Fig. 5a and 5b. The theoretical fitting curves have the $F\beta$ product of 1.1 and 1.2 for the electrical and magnetic dipole modes, which corresponds to the β factors of 0.022 and 0.105, respectively. For comparison, light output curves with two extreme $F\beta$ product values (0.1 and 10) are also shown. The magnetic dipole mode is nondegenerate, and the spontaneous emission couples into a single optical mode, resulting in larger spontaneous emission coupling compared to the degenerate electric dipole mode [26]. The laser wavelength of the electric dipole mode is also detuned from the peak wavelength of the spontaneous emission (~1350 nm, shown in Fig. 4a), which limits the relative amount of spontaneous emission coupled to the cavity mode [26]. Figure 5c and 5d show that the stimulated emission increases rapidly over spontaneous emissions after threshold. Uncoupled spontaneous emission is softly clamped after threshold, confirming that $F\beta$ is large, and spontaneous emission plays an important role in these nanolasers, especially when the quality factor of the cavity is low [27].

5.4. Threshold optical gain and future outlook

The threshold optical gains for the electric and magnetic dipole modes are approximately 695 and 460 cm^{-1}, respectively, according to the rate equation model in Eq. (2). The optical gain coefficient at the laser threshold is inversely proportional to the optical confinement factor and the cavity quality factor, which can be improved by using silver [11, 28] and by optimizing the cavity design and mode profiles [29]. Our numerical simulations predict that the quality factors obtainable using silver nanopatch cavity structures at room temperature are better than our experimentally estimated quality factors based on gold-based cavities operating at low temperature.

Plasmonic effects can be employed to further reduce the effective mode volume and the overall laser dimension especially in the visible wavelength range. However, since the quality factor of a metallic optical cavity is ultimately limited by the material properties of metal regardless of the cavity geometry [30], plasmon-photon mode hybridization or higher gain materials will be necessary to reduce cavity volumes further. Finally, electrically injected lasers based on ultra-thin epitaxial layers is possible with the use of properly engineering ultra-shallow-junctions using monolayer doping of III-V materials [31].

6. Conclusion

We have fabricated and characterized subwavelength-scale nanopatch semiconductor lasers at near infrared wavelengths. Both the effective mode volume and physical size of the nanopatch lasers are kept at subwavelength-scales because of tight optical confinement from metallodielectric resonators. Although compact optical mode volumes are important for obtaining strong light-matter interactions, practically useful laser structures must be physically compact and lend themselves easily to integration with VLSI technology. Contrary to common belief, the presence of metal can *improve* the quality factor of subwavelength

optical resonators by suppressing radiation into free-space. We believe that the nanopatch semiconductor laser can be a strong contender for the integration of optical components with nanoscale electronic devices because they are compact, they are based inherently on wafer-bonding techniques, and they use conductive metal structures for light confinement and electrical carrier injection in an ultra-small footprint.

Acknowledgement